Materials Science in Semiconductor Processing 30 (2015) 197–207

Contents lists available at ScienceDirect

Materials Science in Semiconductor Processing

journal homepage: www.elsevier.com/locate/mssp

Thermoelectric and optoelectronic properties of a heterocyclic isoxazolone nucleus compound

A.H. Reshak [a,b], Sikander Azam [a,*]

[a] New Technologies – Research Center, University of West Bohemia, Univerzitni 8, 306 14 Pilsen, Czech Republic
[b] Center of Excellence Geopolymer and Green Technology, School of Material Engineering, University Malaysia Perlis, 01007 Kangar, Perlis, Malaysia

ARTICLE INFO

Available online 27 October 2014

Keywords:
Density of states
Chemical bonding
Optical properties
Thermo-electric properties

ABSTRACT

The density of states, electronic charge density distribution and the optical susceptibilities of 3-methyl-4-[3-(5-benzyloxy-1H-indole)methylene]-isoxazol-5(4H)-one ($C_{20}H_{16}N_2O_3$) single crystal have been investigated using density functional theory. The exchange-correlation potential was treated within local density approximation (LDA) and the generalized gradient approximation of Perdew–Burke and Ernzerhof (PBE-GGA). In addition, the Engel–Vosko generalized gradient approximation (EV-GGA) was also applied to improve the electronic structure calculations. From the calculated total and partial density of states we concluded that the valence band is dominate by p state of N and C atoms while the conduction band is dominate by p state of N, O and C atoms. We have calculated the optical properties, namely, the real and imaginary parts of the dielectric function, refractive index, extinction coefficient, reflectivity, and energy loss function for radiation up to 14.0 eV. We also calculated the thermoelectric properties of the investigated compound, in order to better understand the temperature dependent, thermal conductivity, the temperature dependence of the Seebeck coefficients and the electrical conductivity for this compound.

1. Introduction

The field of organic electronics has experienced in a few years a rapid development moving from a basic research level to the construction of molecule-based devices that are already commercially viable [1]. These devices have in common that their performance depends on how efficiently the charge carriers are injected and transported in the different organic active layers. Therefore, important advances achieved in this field have been connected to the enhancement of the charge carrier mobility of the organic molecules. However the incorporation of organic molecules in the electronic devices shows still serious stability and processability limitations. At this stage one of the main demands is to find new stable organic semiconducting materials [2].

Isoxazolone nucleus is considered as the best proaromatic acceptor, when associated to aromatic donors, for conjugated donor–acceptor (D–π–A) merocyanine dye [3,4]. Due to their well tunable absorption spectra, molar extinction coefficients, and large first molecular hyperpolarizabilities (β), the merocyanine dyes with an isoxazolone nucleus are being used for the nonlinear optical and optical (recording) research [5]. In 2012 Zhang et al. [6] synthesized, two merocyanine dyes, all with an isoxazolone nucleus. In the two dyes, X-ray crystal structures were correlated with the IR spectra, particularly illustrating the molecular configurations and intra- and inter-molecular

* Corresponding author.
E-mail address: sikander.physicst@gmail.com (S. Azam).

http://dx.doi.org/10.1016/j.mssp.2014.10.005
1369-8001/

connections. The details through the X-ray crystallography resulting about the molecular configuration (or intermolecular interactions) relating to the cyanine and merocyanine dyes are still effective and are a view to their practical application [7]. Interestingly, the derivatives of isoxazolone can be present in three tautomeric forms i.e. in the OH, C═O and also in the NH form. These mixture can be always obtained but usually the most important form is ketonic [8]. The canine derivatives are of particular interest for the chirooptical effects [9]. Zhang et al. [6] focused on the effect of the solvent on the electrical devices absorption of the dyes through experimental and theoretical procedures. The solvatochromism of the dyes was reproduced through the time dependent density functional theory (TDDFT) parallel with the self-consistent reaction field (SCRF) approach, which hinged on the adjacent solvent molecules and a polarizable continuum. This has proved that the theoretical calculations of organic dyes on the chromophoric properties are inevitable apparatus for practical applications and are probably helpful in forecasting and clarifying the structure–property relationships of the dyes [10–13]. Thus, for the IR spectra of the dyes, the resonance frequency calculations were conducted for initial studies. In experimental study the vibrational spectroscopy depicts a directly relation in the spectra and the structure, but the theoretical calculations of vibrational spectra are of practical value for the recognition of identified and unidentified compounds [14–16].

In view of $C_{20}H_{16}N_2O_3$ we found that there is a scarcity of theoretical information. In the past the B3LYP method was used in investigating the vibrational data and electronic spectra of this compound [6]. To the best of our knowledge, no electronic structure, chemical bonding, optical properties and thermal properties of $C_{20}H_{16}N_2O_3$ have been yet reported in literature. Therefore, it stimulates us to deal with the electronic structure, chemical bonding, optical properties and thermal properties of $C_{20}H_{16}N_2O_3$ in the present paper.

The rest of the manuscript has been divided in three parts. In Section 2, we momentarily explain the computational techniques used in this study. In Section 3, which belongs to the results and discussion, the most pertinent results obtained for the electronic structure, chemical bonding, optical properties and the thermoelectric properties of $C_{20}H_{16}N_2O_3$ are presented. In Section 4 we summarized the work.

2. Methodology

The results were carried out within all electron full potential linear augmented plane wave (FPLAPW) method based on DFT [17,18] as implemented in the WIEN2k code [19]. The crystallographic data of the 3-methyl-4-[3-(5-benzyloxy-1H-indole)methylene]-isoxazol-5(4H)-one ($C_{20}H_{16}N_2O_3$) was taken from Cambridge Crystallographic Data Centre, the CCDC number 729689 [20]. The unit cell's

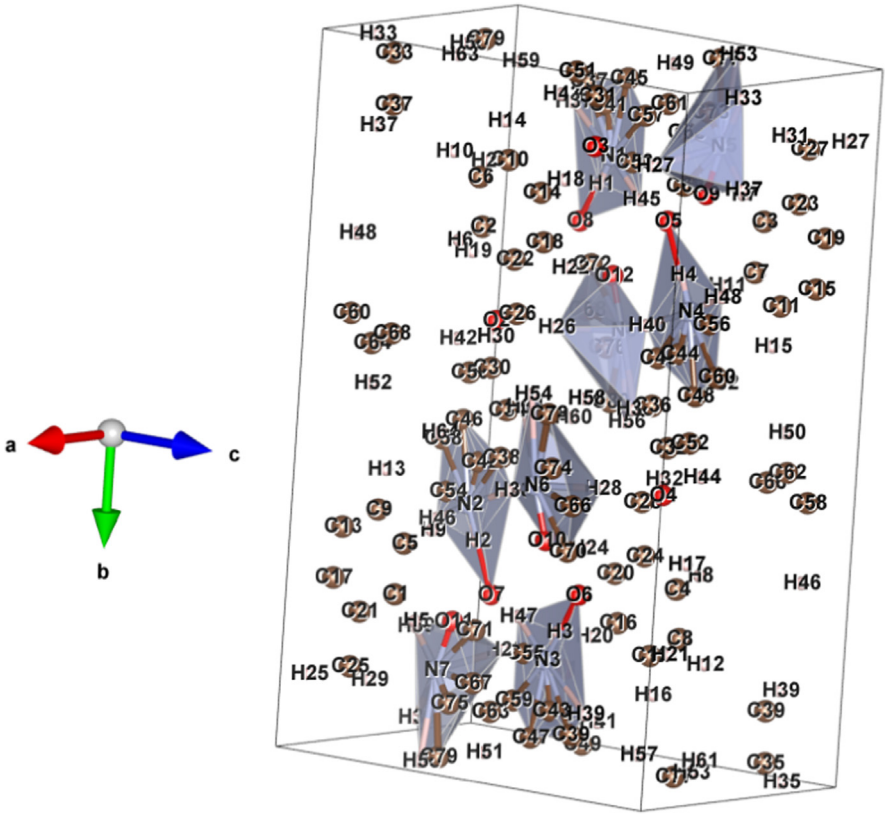

Fig. 1. Unit cell structure of $C_{20}H_{16}N_2O_3$.

structure is illustrated in Fig. 1. The atomic positions were optimized by minimizing the forces acting on each atom. The optimized atomic positions show very good agreement with the experimental data [20]. These are listed in Table 1. The FPLAPW method elaborate the Kohn–Sham orbitals in atomic like orbitals inside the muffin-tin (MT) atomic spheres and plane waves in the interstitial region. The exchange-correlation potential was treated with the local density approximations (LDA) [21] and generalized gradient approximation of Perdew–Burke and Ernzerhof (PBE-GGA) [22]. Furthermore, the Engel–Vosko generalized gradient approximation (EV-GGA) formalism [23] was also implemented in order to get better electronic band structure and optical properties. Such approximation has been illustrated to be fabulous in predicting the band gap energies of bulk materials. A plane-wave cutoff parameter $R_{MT}K_{max}$ equal to 7.0 was used (where R_{MT} is the minimum radius of the muffin-tin spheres and K_{max} gives the magnitude of the largest **k**-vector in the plane wave expansion). The atomic sphere radii of the atoms are taken as; 1.08, 0.54, 1.00, and 1.09 a.u. for C, H, N, and O, respectively. The wave function inside the sphere was expended up to $l_{max} = 10$ and the Fourier expansion of the charge density up to $G_{max} = 26(\text{a.u.})^{-1}$. The self-consistent calculations are converged with the difference in total energy of the crystal did not exceed 10^{-5} Ryd for successive steps. The self-

Table 1
The optimized atomic positions of $C_{20}H_{16}N_2O_3$ in comparison with the experimental one [19].

Parameter			Value			
Crystal system, space group			Monoclinic ($P2_1/n$)			
Unit cell dimensions						
a (Å)			7.3056 (19)			
b (Å)			19.681 (5)			
c (Å)			11.445 (3)			
α (deg)			90.000			
β (deg)			105.063 (4)			
γ (deg)			90.000			
Atoms	Exp. x	Opt. x	Exp. y	Opt. y	Exp. z	Opt. z
N1	0.1561(3)	0.1578	1.17069(10)	0.1720	0.36528(19)	0.3650
H1	0.1256	0.1136	1.2083	0.2173	0.3268	0.3140
N2	0.6610(4)	0.6687	1.09103(12)	0.0907	0.9276(2)	0.9300
O1	0.0264(3)	0.0261	0.90197(8)	0.9020	0.25159(16)	0.2552
O2	0.5201(3)	0.5213	1.21629(9)	0.2195	0.71281(17)	0.7174
O3	0.6463(3)	0.6535	1.16054(9)	0.1627	0.88410(16)	0.8858
C1	−0.0789(5)	0.9237	0.76796(15)	0.7676	0.2526(3)	0.2548
H1A	−0.0387	0.9714	0.7914	0.7958	0.3253	0.3404
C2	−0.1070(5)	0.8950	0.69852(16)	0.6976	0.2537(3)	0.2556
H2	−0.0841	0.9195	0.6755	0.6706	0.3271	0.3428
C3	−0.1684(5)	0.8328	0.66340(15)	0.6622	0.1475(3)	0.1471
H3	−0.1895	0.8077	0.6168	0.6070	0.1485	0.1485
C4	−0.1987(5)	0.8007	0.69730(15)	0.6969	0.0396(3)	0.0374
H4	−0.2388	0.7541	0.6735	0.6694	−0.0327	0.9507
C5	−0.1701(5)	0.8301	0.76639(14)	0.7668	0.0376(3)	0.0366
H5	−0.1914	0.8066	0.7889	0.7936	−0.0362	0.9492
C6	−0.1100(4)	0.8909	0.80273(13)	0.8027	0.1444(2)	0.1452
C7	−0.0876(4)	0.9140	0.87868(13)	0.8787	0.1384(2)	0.1409
H7A	−0.0281	0.9837	0.8902	0.8931	0.0745	0.0683
H7B	−0.2110	0.7716	0.9004	0.9037	0.1207	0.1210
C8	0.0470(4)	0.0481	0.97104(12)	0.9700	0.2691(2)	0.2711
C9	−0.0281(4)	0.9709	1.01931(13)	0.0184	0.1799(2) 0	0.1809
H9	−0.0974	0.8877	1.0051	0.0029	0.1037	0.0903
C10	−0.0004(4)	0.9994	1.08780(13)	0.0877	0.2037(2)	0.2038
H10	−0.0510	0.9348	1.1202	0.1248	0.1451	0.1329
C11	0.1044(4)	0.1075	1.10637(12)	0.1072	0.3169(2)	0.3174
C12	0.1815(4)	0.1855	1.05916(12)	0.0594	0.4078(2)	0.4090
C13	0.1504(4)	0.1555	0.99022(12)	0.9903	0.3832(2)	0.3857
H13	0.1982	0.2125	0.9578	0.9510	0.4424	0.4541
C14	0.2591(4)	0.2619	1.16573(12)	0.1677	0.4793(2)	0.4790
H14	0.3083	0.3181	1.2023	0.2125	0.5290	0.5339
C15	0.2826(4)	0.2860	1.09720(12)	0.0984	0.5135(2)	0.5148
C16	0.3779(4)	0.3802	1.06802(12)	0.0692	0.6240(2)	0.6254
H16	0.3652	0.3674	1.0210	0.0131	0.6247	0.6269
C17	0.4857(4)	0.4873	1.09336(12)	0.0959	0.7313(2)	0.7337
C18	0.5437(4)	0.5475	1.16228(13)	0.1645	0.7663(2)	0.7701
C19	0.5682(4)	0.5715	1.05450(14)	0.0555	0.8378(2)	0.8385
C20	0.5566(4)	0.5573	0.97953(14)	0.9805	0.8507(2)	0.8503
H20A	0.6321	0.6407	0.9660	0.9636	0.9291	0.9409
H20B	0.6030	0.61287660	0.9576	0.9542	0.7892	0.7806
H20C	0.4271	0.40741778	0.9666	0.9647	0.8423	0.8392

consistency was obtained using 500 **k** points in irreducible Brillouin zone (IBZ) using the Monkhorst–Pack particular **k**-points approach [24].

In general, the optical properties of the matter may be drawn from the knowledge of the complex dielectric function $\varepsilon(\omega)=\varepsilon_1(\omega)+i\varepsilon_2(\omega)$. The imaginary part $\varepsilon_2(\omega)$ is a natural output of the electronic band structure calculations, while the real part $\varepsilon_1(\omega)$ can be obtained using Kramers–Kronig relation [25]. The other related optical constants, like the refractive index $n(x)$, extinction coefficient $k(x)$, optical reflectivity $R(\omega)$, and the energy-loss spectrum $L(\omega)$, can be computed from the existing information about $\varepsilon_2(\omega)$ and $\varepsilon_1(\omega)$ [26,27]. For computing the optical properties, a dense mesh of uniformly distributed **k**-points is used, the BZ integration was performed using a $10\times10\times10$ **k**-mesh.

We have employed the BoltzTraP code [28] to investigate the thermoelectric properties supported by the analytical expressions of the electronic band structure. The method for calculating the transport properties of a crystalline solid is based on the semi-classical Boltzmann theory and the rigid band approach. This approach has been used in rationalizing and envisaging the optimal doping level of known compounds [29–31]. The rigid band approach to conductivity is based on the transport distribution, which is the kernel of all transport coefficients. The transport distribution is defined as [32,33]

$$\Xi=\sum_{\vec{k}}\vec{v}_{\vec{k}}\vec{v}_{\vec{k}}\vec{\tau}_{\vec{k}}\ldots\ldots\ldots\ldots \quad (1)$$

where $\vec{v}_{\vec{k}}$ is the group velocity associated with that state and $\vec{\tau}_{\vec{k}}$ is the relaxation time.

3. Results and discussions

3.1. Density of states

In this section, we turn our attention to study the total and partial density of states of $C_{20}H_{16}N_2O_3$. In order to demonstrate the effect of using different exchange correlation potentials we

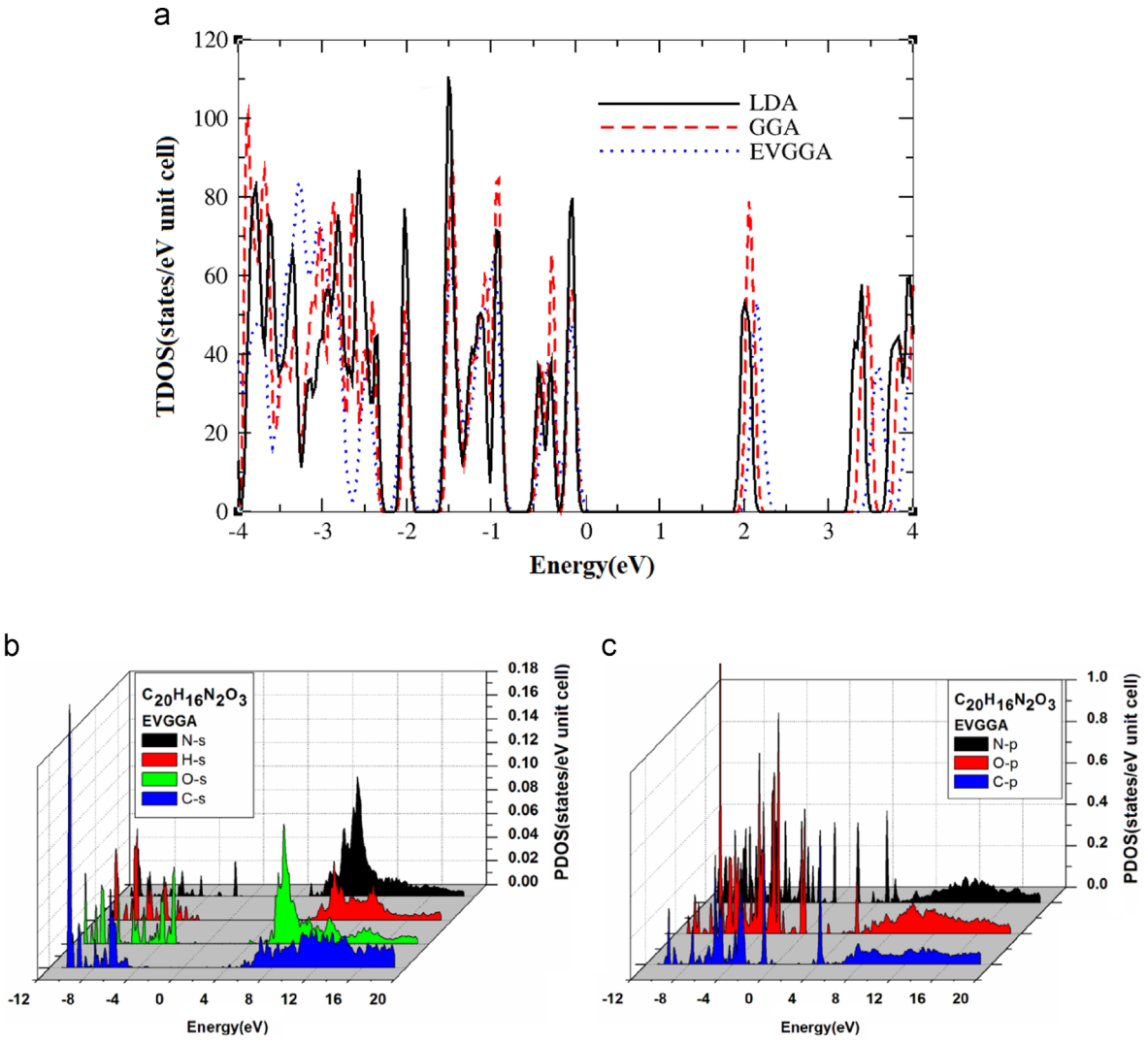

Fig. 2. Calculated total and partial densities of states (states/eV unit cell).

have plotted the total density of states (TDOS) using LDA, GGA and EVGGA as illustrated in Fig. 2a. The calculated band gaps are 1.93 (LDA), 1.99 (GGA) and 2.08 (EVGGA). We found that EVGGA shows better results than LDA and GGA; thus we decided to demonstrate the partial density of states (PDOS) obtained by EVGGA as illustrated in Fig. 2b and c. It is well know that LDA and GGA approaches have simple forms that are not sufficiently flexible to accurately reproduce both the exchange-correlation energy and its charge derivative. Engel and Vosko considered this shortcoming and constructed a new functional form of GGA that is able to better reproduce the exchange potential at the expense of less agreement in the exchange energy. This approach, called EV-GGA, yields better band splitting and some other properties that mainly depend on the accuracy of the exchange-correlation potential [34–46]. Fig. 2 suggest that the TDOS and PDOS are divided into five

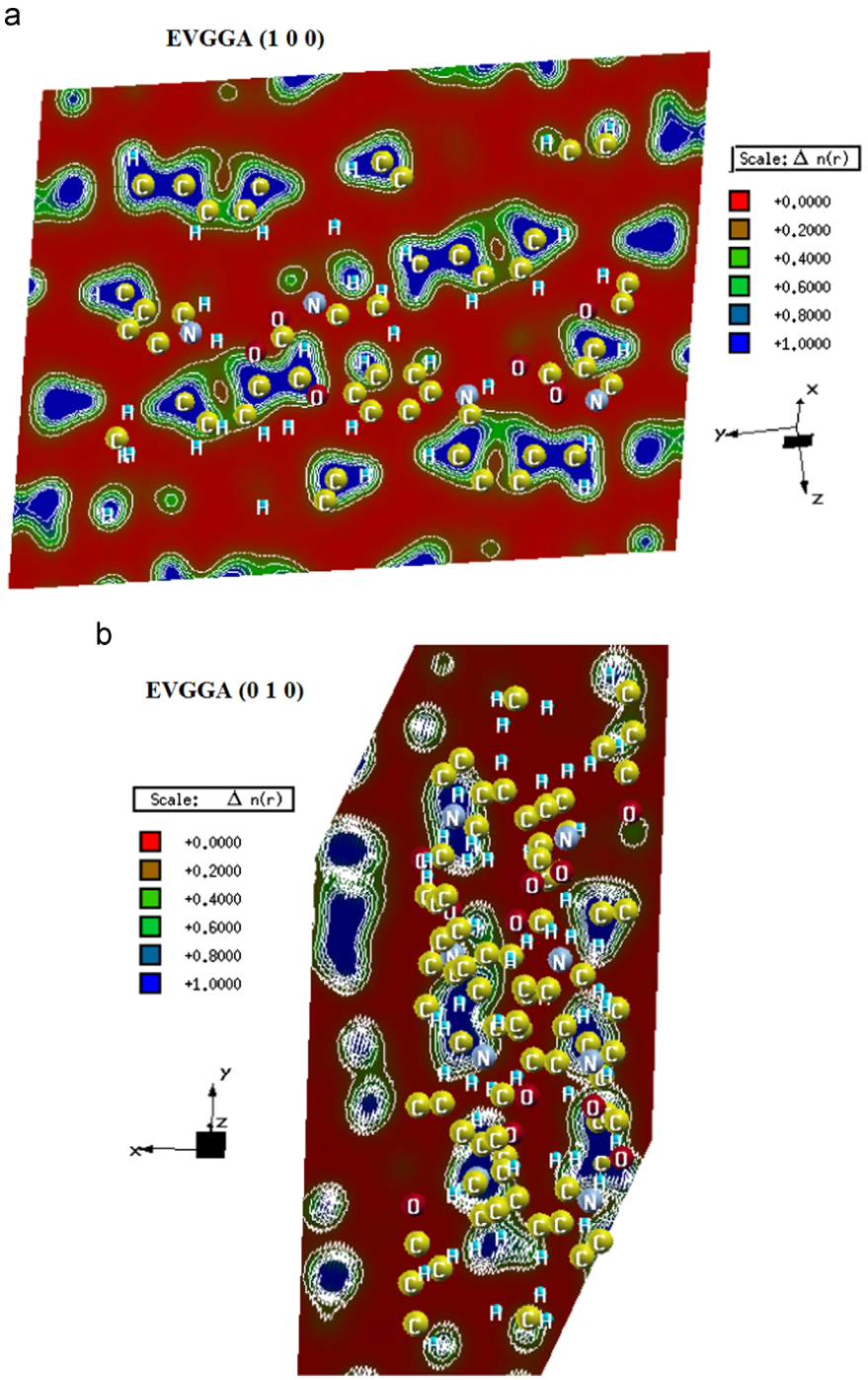

Fig. 3. Electronic charge density contour in (100) and (001) planes. (For interpretation of the references to color in this figure, the reader is referred to the web version of this article.)

distinct structures. Starting from the lower energies, the structure situated between −11.0 and −6.0 eV originates from O-p states with admixture of N-s/p, C-s/p, O-s and H-s states. It is clear that N-s and H-s and also N-s and O-s indicate a strong hybridization, resulting in covalent bonding. The second structure lying between −6.0 and -3.0 eV consists of O-p states with small contribution of N-s/p, C-p, H-s and O-s states. The bands lying from −3.0 eV up to Fermi level (E_F) are mainly comprised of O-p and C-p states with a small contribution from N-s/p states. The minimum conduction band at 2.0 eV consists entirely of N-p states. The conduction bands from 3.5 up to 18.0 eV are contributed mainly by p-states of C, N and O atoms. There is strong hybridization between N-p and O-p states in the conduction band. The valence band is dominated by the p state of N and C atoms while the conduction band is dominated by the p state of N, O and C atoms.

In order to further explore the bonding nature in $C_{20}H_{16}N_2O_3$, the electronic charge distribution is examined. The contour of the charge density in (100) plane containing carbon, hydrogen, oxygen and nitrogen atoms is shown in Fig. 3. Furthermore, the charge transfer between cations and anions exists, which indicates an ionic contribution to the bonding. Thus, the bonding in $C_{20}H_{16}N_2O_3$ may be expressed as a mixture of covalent-ionic behavior.

We also have calculated the electronic charge density in (001) crystallographic plane in order to explore the anisotropy in the electronic charge density distribution. As it is clear from the two planes that nitrogen atom does not appear in (100) plane while it appears in the (001) plane. In (100) plane the oxygen atom forms a covalent bonding with carbon atom while in the (001) plane oxygen atom forms ionic bonding. The thermoscale shows the intensity of the charge density round the atoms in which the blue color shows maximum charge while the red color shows zero charge density. The calculated bond lengths and angles show very good agreement with the experimental data [20] (see Tables 2 and 3).

3.2. Dispersion of optical properties

An understanding of the electronic structures can be reached by investigating the optical spectra, which not only give information about the occupied and unoccupied states, but also about the features of the bands [47,48]. Optical spectroscopy analysis is a powerful tool for determining the overall band behavior of a solid [49]. The energy eigenvalues and electron wave function are required to calculate the frequency-dependent dielectric function [50–52]. We have calculated the dispersion of the optical properties using the EVGGA approximation for the energy up to 14.0 eV. The real $\varepsilon_1(\omega)$ and imaginary $\varepsilon_2(\omega)$ parts of the dielectric function are illustrated in Fig. 4a and b. The imaginary part $\varepsilon_2(\omega)$ is directly interrelated to the band structure of the material and portrays its absorptive performance. We should emphasize that only the direct transitions which conserve the crystal momentum are incorporated in the calculated optical properties. Indirect transitions such as those assisted by lattice vibrations are excluded and found to have very small effect on the absorption edge. As the under studied compound has the monoclinic symmetry, therefore it has five nonzero components of the second-order dielectric tensor,

Table 2
The calculated bond lengths in Å of $C_{20}H_{16}N_2O_3$ in comparison with the experimental one [19].

Bonds	Exp.	Opt.	Bonds	Exp.	Opt.
N1–C14	1.330(3)	1.332	C7–H7A	0.9700	1.118
N1–C11	1.394(3)	1.397	C7–H7B	0.9700	1.120
N1–H1	0.8600	1.068	C8–C13	1.381(3)	1.400
N2–C19	1.293(3)	1.300	C8–C9	1.398(3)	1.411
N2–O3	1.450(3)	1.499	C9–C10	1.380(4)	1.395
O1–C8	1.377(3)	1.356	C9–H9	0.9300	1.100
O1–C7	1.422(3)	1.427	C10–C11	1.372(3)	1.388
O2–C18	1.216(3)	1.229	C10–H10	0.9300	1.102
O3–C18	1.362(3)	1.350	C11–C12	1.400(3)	1.414
C1–C6	1.381(4)	1.397	C12–C13	1.392(3)	1.391
C1–C2	1.383(4)	1.394	C12–C15	1.450(3)	1.400
C1–H1A	0.9300	1.101	C13–H13	0.9300	1.103
C2–C3	1.369(4)	1.393	C14–C15	1.402(3)	1.422
C2–H2	0.9300	1.103	C14–H14	0.9300	1.098
C3–C4	1.369(5)	1.395	C15–C16	1.398(3)	1.396
C3–H3	0.9300	1.103	C16–C17	1.369(3)	1.386
C4–C5	1.377(4)	1.392	C16–H16	0.9300	1.109
C4–H4	0.9300	1.103	C17–C19	1.432(3)	1.437
C5–C6	1.386(4)	1.399	C17–C18	1.446(3)	1.448
C5–H5	0.9300	1.104	C19–C20	1.488(4)	1.489
C6–C7	1.507(4)	1.507	C20–H20A	0.9600	1.108
C20–H20B	0.9600	1.112	C20–H20C	0.9600	1.113

only $\varepsilon_2^{xx}(\omega)$, $\varepsilon_2^{yy}(\omega)$ and $\varepsilon_2^{zz}(\omega)$ are the major components, these are the imaginary parts of the frequency-dependent dielectric function.

Our analysis of $\varepsilon_2(\omega)$ spectrum shows that the first critical point (threshold energy) of the dielectric function occurs at about 1.60 eV for $\varepsilon_2^{xx}(\omega)$, $\varepsilon_2^{yy}(\omega)$ and $\varepsilon_2^{zz}(\omega)$. The critical point is the direct optical transition between the highest valence band and the lowest conduction band. This is known as the fundamental absorption edge. Beyond this point, the curve increases rapidly. This peak is probably related to the interband transition from occupied states with predominantly N-p to unoccupied O-p states. For the real part $\varepsilon_1(\omega)$ spectrum the main peak is located at about 2.0 eV. The curve shows a decrease followed by an increase and then decreases to reach negative value; followed by a slow increase toward zero at high energy. The negative values of $\varepsilon_1(\omega)$ correspond to the local maxima of reflectivity as shown in Fig. 4d. The calculated static dielectric constant is found to be equal to 2.44, 3.28 and 3.71, for $\varepsilon^{xx}(0)$,$\varepsilon^{yy}(0)$ and $\varepsilon^{zz}(0)$, respectively.

The refractive index is displayed in Fig. 4c. The static refractive index $n(0)$ is found to have the values 1.56, 1.80 and 1.91 for $n^{xx}(\omega)$,$n^{yy}(\omega)$ and $n^{zz}(\omega)$, respectively. It increases with energy in the transparency region to form a peak in the ultraviolet at about 1.8 eV. Then it decreases to a minimum level at 5.5 eV. The origin of the structures in the imaginary part of the dielectric function also explains the structures in the refractive index. The variation of reflectance as a function of photon frequency $R^{xx}(\omega)$, $R^{yy}(\omega)$ and $R^{zz}(\omega)$ is displayed in Fig. 4d. The dynamic reflectance corresponds to the ratio of the intensities of the incident and reflected electric fields. In the low energy regime <1.5 eV the reflectance is small, and the static reflectivity $R(0)$ values of $R^{xx}(0)$,$R^{yy}(0)$ and $R^{zz}(0)$ are 0.05, 0.08 and 0.1, respectively. The small value of reflectance ensures its applications as transparent coatings in the visible light regime. $C_{20}H_{16}N_2O_3$ shows an overall

Table 3
The calculated bond angles in (deg) of $C_{20}H_{16}N_2O_3$ in comparison with the experimental one [19].

Angles	Exp.	Opt.	Bonds	Exp.	Opt.
C14–N1–C11	110.4(2)	110.38	C16–C15–C12	124.6(2)	123.97
C14–N1–H1	124.8	127.12	C14–C15–C12	105.4(2)	105.49
C11–N1–H1	124.8	122.49	C17–C16–C15	134.2(2)	133.30
C19–N2–O3	105.9(2)	104.72	C17–C16–H16	112.9	113.14
C8–O1–C7	117.83(19)	117.44	C15–C16–H16	112.9	113.56
C18–O3–N2	109.64(18)	109.28	C16–C17–C19	125.8(2)	123.90
C6–C1–C2	120.5(3)	120.25	C16–C17–C18	130.5(2)	132.00
C6–C1–H1A	119.7	119.38	C19–C17–C18	103.7(2)	104.07
C2–C1–H1A	119.7	120.37	O2–C18–O3	119.3(2)	118.82
C3–C2–C1	120.4(3)	120.19	O2–C18–C17	133.4(2)	133.09
C3–C2–H2	119.8	120.26	O3–C18–C17	107.3(2)	108.08
C1–C2–H2	119.8	119.55	N2–C19–C17	113.4(3)	113.84
C4–C3–C2	119.6(3)	119.85	N2–C19–C20	120.3(2)	119.38
C4–C3–H3	120.2	120.37	C17–C19–C20	126.3(2)	126.78
C2–C3–H3	120.2	119.78	C19–C20–H20A	109.5	110.36
C3–C4–C5	120.4(3)	119.96	C19–C20–H20B	109.5	110.44
C3–C4–H4	119.8	120.64	H20A–C20–H20B	109.5	108.43
C5–C4–H4	119.8	119.40	C19–C20–H20C	109.5	110.87
C4–C5–C6	120.6(3)	120.47	H20A–C20–H20C	109.5	108.00
C4–C5–H5	119.7	119.38	H20B–C20–H20C	109.5	108.65
C6–C5–H5	119.7	120.00	C10–C9–H9	119.7	117.89
C1–C6–C5	118.4(3)	119.29	C8–C9ϖH9	119.7	121.41
C1–C6–C7	122.5(2)	121.71	C11–C10–C9	117.7(2)	122.48
C5–C6–C7	119.0(2)	118.98	C11–C10–H10	121.2	122.48
O1–C7–C6	108.8(2)	109.33	C9–C10–H10	121.2	119.61
O1–C7–H7A	109.9	109.63	C10–C11–N1	130.1(2)	130.18
C6–C7–H7A	109.9	110.64	C10–C11–C12	122.9(2)	122.08
O1–C7–H7B	109.9	109.05	N1–C11–C12	107.0(2)	107.73
C6–C7–H7B	109.9	109.76	C13–C12–C11	118.9(2)	119.69
H7A–C7–H7B	108.3	108.40	C13–C12–C15	133.8(2)	133.83
O1–C8–C13	114.8(2)	115.26	C11–C12–C15	107.3(2)	106.48
O1–C8–C9	123.9(2)	123.87	C8–C13–C12	118.6(2)	118.74
C13–C8–C9	121.3(2)	120.87	C8–C13–H13	120.7	118.69
C10–C9–C8	120.7(2)	120.70	C12–C13–H13	120.7	122.56
N1–C14–C15	110.0(2)	109.92	C15–C14–H14	125.0	127.27
N1–C14–H14	125.0	122.81	C16–C15–C14	130.0(2)	130.53

larger reflectance in the range of 2.0–6.3 eV and also at the higher energy. The electron energy loss function $L(\omega)$ is an important factor describing the energy loss of a fast electron traversing in a material. The prominent peaks in $L^{xx}(\omega)$, $L^{yy}(\omega)$ and $L^{zz}(\omega)$ spectra represent the characteristic associated with the plasma resonance (a collective oscillation of the valence electrons) and the corresponding frequency is the so-called plasma frequency ω_p. The peaks of $L(\omega)$ correspond to the trailing edges in the reflection spectra $R(\omega)$. For instance the prominent peak of $L^{xx}(\omega)$, $L^{yy}(\omega)$ and $L^{zz}(\omega)$ are located at 2.48, 6.19 and 6.32 eV, respectively (Fig. 4e) are at an energy corresponding to the abrupt reduction of $R(\omega)$ (Fig. 4d). From above we would like to mention here that there is a considerable anisotropy among the three tensor components of all the optical properties.

3.3. Thermoelectric properties

3.3.1. Electronic transport properties

During the 1990s there was a heightened interest in the field of thermoelectrics driven by the need for more efficient materials for electronic refrigeration and power generation [53–56]. Proposed industrial and military applications of thermoelectric (TE) materials are generating increased activity in this field by demanding higher performance, near room-temperature TE materials than those presently in use. Thermoelectric refrigeration is an environmentally "green" method of small-scale localized cooling in computers, infrared detectors, electronics, and opto-electronics as well as many other applications. However, most of the electronics and optoelectronics technologies typically require only small scale or localized spot cooling of small components which do not impose a large heat load. Thermoelectric materials, which involve direct conversion between heat and electrical energy with electrons or holes as energy carriers, have attracted great interest in the past few decades [57,58]. The efficiency of a thermoelectric material is usually characterized by the dimensionless thermoelectric figure of merit (ZT). Materials with high electrical conductivity, large Seebeck coefficient and low thermal conductivity are preferred for practical applications.

Semiconductors are ideal thermoelectric devices because of their band structure and electronic properties at high temperatures. Fig. 5 illustrates the transport properties versus chemical potential at three different temperatures. While the magnitude of the Seebeck coefficient (Fig. 5a) is reduced with increasing temperature at a certain chemical potential, the electrical conductivity over relaxation time (σ/τ) (Fig. 5b) is decreased whereas the electronic thermal conductivity over relaxation time ($\breve{k}_e/\tau$) (Fig. 5c) increases with increasing temperature in the displayed chemical

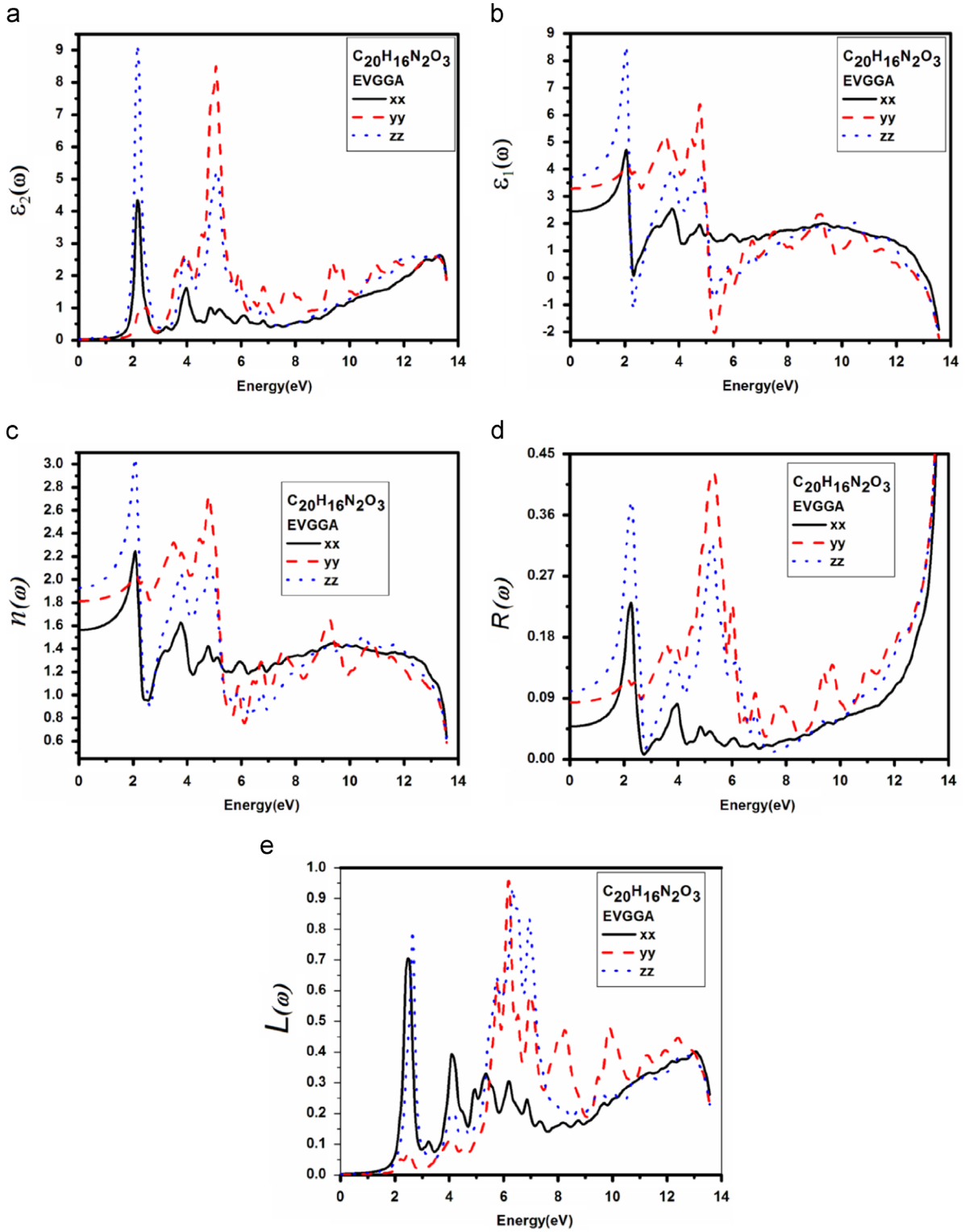

Fig. 4. Calculated imaginary part $\varepsilon_2^{xx}(\omega)$ (dark solid curve-black color), $\varepsilon_2^{yy}(\omega)$ (long dashed curve-red color) and $\varepsilon_2^{zz}(\omega)$ (dotted-blue color) spectra; calculated real part $\varepsilon_1^{xx}(\omega)$ (dark solid curve-black color), $\varepsilon_1^{yy}(\omega)$ (long dashed curve-red color) and $\varepsilon_1^{zz}(\omega)$ (dotted-blue color) spectra; Calculated energy-loss spectrum $L^{xx}(\omega)$ (dark solid curve-black color), $L^{yy}(\omega)$ (long dashed curve-red color) and $L^{zz}(\omega)$ (dotted-blue color) spectra; Calculated reflectivity $R^{xx}(\omega)$ (dark solid curve-black color), $R^{yy}(\omega)$ (long dashed curve-red color) and $R^{zz}(\omega)$ (dotted-blue color) spectra; and Calculated refractive index $n^{xx}(\omega)$ (dark solid curve-black color), $n^{yy}(\omega)$ (long dashed curve-red color) and$n^{zz}(\omega)$ (dotted-blue color) spectra. (For interpretation of the references to color in this figure legend, the reader is referred to the web version of this article.)

potential range. To calculate systematically the temperature dependent properties, a series of transport properties versus chemical potential curves were calculated by varying the temperature. After obtaining the chemical potential at a specific temperature from Eq. (1), one can determine the values of S, σ/τ, $\breve{k}_e/\tau$ and $S^2\sigma/\tau$ at specific temperature from the corresponding curve.

3.3.2. Seebeck coefficients

Thermoelectric properties are capable of converting heat directly into electricity. They are based on the Seebeck effect discovered by Thomas Johann Seebeck in 1821. Fig. 5a represents the calculated temperature-dependent Seebeck coefficients of the investigated compound. The chemical potential dependence on the electrical transport properties of $C_{20}H_{16}N_2O_3$ was calculated at three different temperatures 300 K, 500 K and 700 K as shown in Fig. 5a. Within the rigid-band shift model, the chemical potential μ determines the carrier concentration of the compound. The Seebeck coefficients are negative and also positive in the investigated temperature range, signifying both elect ron and hole-type carriers but the holes dominate the heat transport in these materials. The value of S has some dynamic behavior if we look to the Seebeck coefficient plot; it is clear that at low temperature i.e. at 300 K the Seebeck coefficient plot is much flat at the center but with increase in the temperature to 500 or 700 K the flatness disappears with significant decrease in the peaks of the Seebeck coefficient.

The investigated compound has larger Seebeck coefficient at temperature around 300 K. Generally, the compounds with large Seebeck coefficient show the large contrast of DOS and/or carriers (electrons and holes) velocities above/below the chemical potential, especially near to the band gap edges. As we see that with increasing the temperature from 300 to 500 K and then from 500 to 700 K, the peaks decrease showing that the thermoelectric properties of the investigated compound are decreasing. The highest peak for the investigated compound occurs at 0.28, which shows that this material has the maximum hole concentration, that is attributed to the fact that the maximum peak shows the greater thermoelectric property of the material.

3.3.3. Electrical conductivity

Within the framework of the Boltzmann transport equation at constant relaxation time (τ) approximation, the electrical conductivity (σ) is expressed in the form of

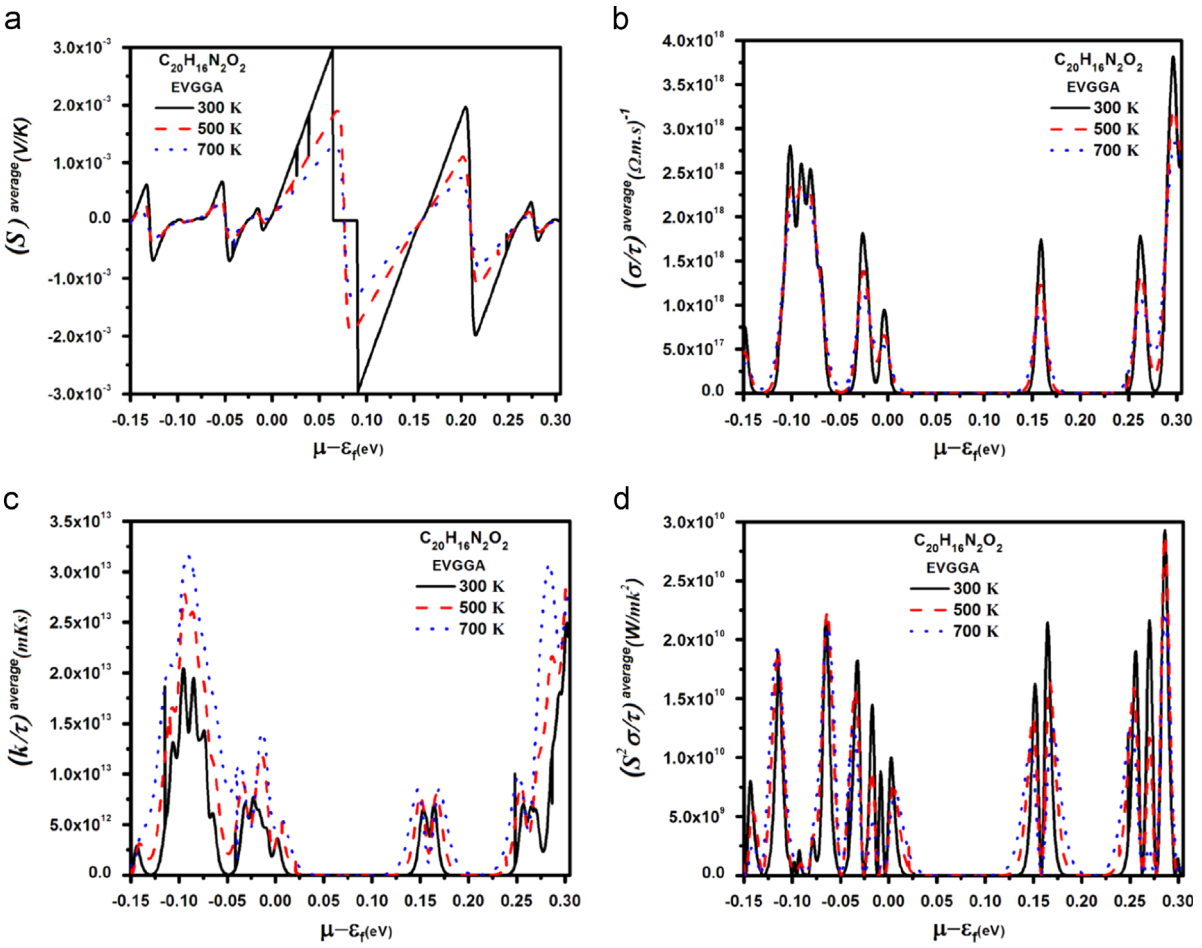

Fig. 5. Calculated thermoelectric properties i.e. Seebeck coefficients, electrical conductivity, thermal conductivity and the power factor.

the ratio σ/τ. To calculate the electrical conductivity σ, we must determine the relaxation time τ. We assume that the relaxation time τ is direction independent, and treat the relaxation time as a constant at a certain specific temperature and carrier concentration. Fig. 5b shows the calculated electrical conductivity. The results follow the trend that the electrical conductivity decreases with increasing temperature and it exhibits metal-like behavior.

3.3.4. Thermal conductivity

In metals thermal conductivity approximately tracks electrical conductivity according to the Wiedemann–Franz law [59]; the freely moving valence electron is not only transferring the electric current but also heat energy. However, the general correlation between electrical and thermal conductance does not hold for other materials, due to the increased importance of phonon carriers for heat in non-metals. Thermal conductivity is imperative in material science, research, electronics, building insulation and related fields, particularly where high operating temperatures are achieved. High energy generation rates within electronics or turbines require the use of materials with high thermal conductivity. The thermal conductivity, (k/τ), indicates the ability of a material to conduct heat for both electronic and lattice contributions. Thus, the thermal conductivity of a material is the sum of its electronic and the corresponding lattice thermal conductivities. In Fig. 5c, we illustrated the thermal conductivity (k/τ) for the investigated compound. The temperature characteristic of thermal conductivity (k/τ) of $C_{20}H_{16}N_2O_3$ exhibits the most peculiar features in all measured thermoelectric properties. The figure shows that as we increase the temperature from 300 K the thermal conductivity increases, which shows that the investigated material does not possess good electrical properties.

3.3.5. Power factor

The Seebeck coefficient is not the only number that determines the usefulness of a material in a thermoelectric generator or a thermoelectric cooler. Under a given temperature coolness, the ability of a material to produce useful electrical power is quantified by its power factor,

$$PF = S^2\sigma \quad (2)$$

where S is Seebeck coefficient and σ is the electrical conductivity. Material with high power factor is able to generate more energy in a space-constrained application, but they are not necessarily efficient. Fig. 5d shows the temperature dependent power factor decreases when we increase temperature above 300 K. That means that the investigated compound shows good thermoelectric properties at room temperature.

4. Conclusions

This study reports a detailed investigation on the electronic, optical, and thermal properties of 3-methyl-4-[3-(5-benzyloxy-1H-indole)methylene]-isoxazol-5(4H)-one ($C_{20}H_{16}N_2O_3$) using first-principles PFLAPW method within LDA, GGA and EV-GGA potential. From the TDOS and PDOS study we concluded that the valence band is dominated by the p state of N and C atoms while the conduction band is dominated by the p state of N, O and C atoms. We calculated the electronic charge density in the (100) plane in order to explore the bonding nature of the investigated compound. We also calculated the electronic charge density in the (001) plane to discuss the anisotropy in the two planes of the crystal. The optical parameters such as the refraction index, dielectric constant, reflectivity, and the energy loss function are calculated and analyzed in this paper. The prominent variations in the optical parameters make $C_{20}H_{16}N_2O_3$ suitable for optical devices due to the small value of reflectance which ensures its application as transparent coatings in the visible light regime, also due to the existence of the considerable anisotropy among the three tensor components of all the optical properties. In this work, an effort was made to use the first principles calculations in combination with the empirical approaches to envisage and understand the thermal electric properties of $C_{20}H_{16}N_2O_3$ and to investigate the possibility of using such material as thermoelectric materials which can convert the heat directly into electricity. The negative and positive signs of the Seebeck coefficients in the investigated temperature range signify that both electron and hole-type carriers and the holes dominate the heat transport in these materials.

Acknowledgment

The result was developed within the CENTEM project, Reg. no. CZ.1.05/2.1.00/03.0088, co-funded by the ERDF as part of the Ministry of Education, Youth and Sports OP RDI program. Computational resources were provided by MetaCentrum (LM2010005) and CERIT-SC (CZ.1.05/3.2.00/08.0144) infrastructures.

References

[1] H. Klauk, Organic Electronics, Wiley-VCH, Weinheim, 2006. K. Müllen, U. Scherf, Organic Light-Emitting Devices. Synthesis, Properties and Applications, Wiley-VCH, Weinheim, 2006.
[2] M. Eva, Enrique Gutierrez-Puebla, M. Angeles Monge, Rafael Ramírez , Pedro de Andrés, Alicia de Andrés, Rafael Ramírez, Berta Gómez-Lor, vol. 10, 2009, pp. 643–652.
[3] E. Aret, H. Meekes, E. Vlieg, G. Deroover, Dyes Pigment. 72 (2007) 339–344.
[4] M.A. Deij, J.Ht. Horst, H. Meekes, P. Jansens, E. Vlieg, J. Phys. Chem. B 111 (2007) 1523–1530.
[5] S. Alías, R. Andreu, M.J. Blesa, M.A. Cerdán, S. Franco, J. Garín, et al., J. Org. Chem. 73 (2008) 5890–5898.
[6] X.-H. Zhang, et al., Dyes Pigment. 93 (2012) 1408–1415.
[7] J.E. Lee, H.J. Kim, M.R. Han, S.Y. Lee, W.J. Jo, S.S. Lee, et al., Dyes Pigment. 80 (2009) 181–186.
[8] S.A. Laufer, S. Margutti, J. Med. Chem. 51 (8) (2008) 2580–2584.
[9] C. Andraud, I.V. Kityk, H. Kutawara,G. Lemercier, K. Stromberger, M. Alexandre, W. Gruhn, K.S. Pak, vol. 57, 2003, pp. 1489–1495.
[10] T. Kolev, T. Tsanev, S. Kotov, H. Mayer-Figge, M. Spiteller, W.S. Sheldrick, et al., Dyes Pigment. 82 (2009) 95–101.
[11] D. Casanova, F.P. Rotzinger, M. Grätzel, J. Chem. Theory Comput. 6 (4) (2010) 1219–1227.
[12] J. Preat, J. Phys. Chem. C 114 (39) (2010) 16716–16725.
[13] K. Meguellatia, S. Ladamea, M. Spichty, Dyes Pigment. 90 (2) (2011) 114–118.
[14] Y.L. Fu, W. Huang, C.L. Li, L.Y. Wang, Y.S. Wei, Y. Huang, et al., Dyes Pigment. 82 (2009) 409–415.
[15] D. Sajan, N. Vijayan, K. Safakath, R. Philip, I.H. Joe, J. Phys. Chem. A 115 (29) (2011) 8216–8226.

[16] B. Rieff, S. Bauer, G. Mathias, P. Tavan, J. Phys. Chem. B 115 (9) (2011) 2117–2123.
[17] K.M. Wong, S.M. Alay-e-Abbas, A. Shaukat, Y. Fang, Y. Lei, J. Appl. Phys. 113 (2013) 014304.
[18] K.M. Wong, S.M. Alay-e-Abbas, A. Shaukat, Y. Fang, Y. Lei, J. Appl. Phys. 114 (2013) 034901.
[19] P. Blaha, K. Schwarz, G.K.H. Madsen, D. Kvasnicka, J. Luitz, WIEN2k: An Augmented Plane Wave Local Orbitals Program for Calculating Crystal Properties, Karlheinz Schwarz/Technical Universität Wien, Wien, 2001.
[20] X.H. Zhang, Yong-Hua Zhan, Dan Chen, Fu Wang, Lan-Ying Wang Dyes Pigment. 93 (2012) 1408-1415.
[21] J.P. Perdew, A. Zunger, Phys. Rev. B 23 (1981) 5048.
[22] J.P. Perdew, K. Burke, M. Ernzerhof, Phys. Rev. Lett. 77 (1996) 3865.
[23] E. Engel, S.H. Vosko, Phys. Rev. B 50 (1994) 10498.
[24] H.J. Monkhorst, J.D. Pack, Phys. Rev. B 13 (1976) 5188.
[25] C. Ambrosch-Draxl, J.O. Sofo, Comput. Phys. Commun. 175 (2006) 1.
[26] A. Delin, A.O. Eriksson, R. Ahuja, B. Johansson, M.S.S. Brooks, T. Gasche, S. Auluck, J.M. Wills, Phys. Rev. B 54 (1996) 1673.
[27] Y.P. Yu, M. Cardona, Fundamentals of Semiconductors: Physics and Materials Properties, 2nd edn. Springer, Berlin, 1999, 233.
[28] G.K.H. Madsen, D.J. Singh, Comput. Phys. Commun. 175 (2006) 67–71.
[29] P.B. Allen, in: J.R. Chelikowsky, S.G. Louie (Eds.), Quantum Theory of Real Materials, Kluwer, Boston, 1996, pp. 219–250.
[30] W. Wei, Z.Y. Wang, L.L. Wang, H.J. Liu, R. Xiong, J. Shi, H. Li, X.F. Tang, J. Phys. D: Appl. Phys. 42 (2009) 115403.
[31] S. Johnsen, A. Bentien, G.K.H. Madsen, B.B. Iversen, M. Nygren, Chem. Mater. 18 (2006) 4633.
[32] A. Qiu, L. Zhang, A. Shan, J. Wu, Phys. Rev. B 77 (2008) 205207.
[33] T.J. Scheidemantel, C. Ambrosch-Drax, T. Thonhauser, J.V. Badding, J.O. Sofo, Phys. Rev. B 68 (2003) 125210.
[34] A.H. Reshak, S. Azam, J. Magn. Magn. Mater. 352 (2014) 72–80.
[35] A.H. Reshaka, B. Wilayat Khan, J. Alloys Compd. 591 (2014) 362–369.
[36] S.A. Khan, A.H. Reshak, Int. J. Electrochem. Sci. 8 (2013) 9459–9473.
[37] A.H. Reshak, S.A. Khan, S. Auluck, RSC Adv. 4 (2014) 6957–6964.
[38] A.H. Reshak, S.A. Khan, Mater. Res. Bull. 48 (2013) 4555–4564.
[39] A.H. Reshak, S.A. Khan, J. Alloys Compd. 595 (2014) 125–130.
[40] A.H. Reshak, S. Azam, J. Magn. Magn. Mater. 362 (2014) 204–215.
[41] A.H. Reshak, et al., J. Magn. Magn. Mater. 363 (2014) 133–139.
[42] A.H. Reshak, S. Azam, J. Magn. Magn. Mater. 358–359 (2014) 16–22.
[43] A.H. Reshak, S. Azam, J. Magn. Magn. Mater. 351 (2014) 98–103.
[44] A.H. Reshak, S. Azam, Int. J. Electrochem. Sci. 8 (2013) 10359–10375; A.H. Reshak, S. Azam, J. Magn. Magn. Mater. 352 (2014) 72–80.
[45] S. Azam, A.H. Reshak, Physica B 431 (2013) 102–108.
[46] S. Azam, A.H. Reshak, J. Organomet. Chem. 766 (2014) 22–33.
[47] S. Azam, A.H. Reshak, Solid State Sci. 32 (2014) 26–34.
[48] S. Azam, A.H. Reshak, RSC Adv. 4 (2014) 20102–20113.
[49] S. Azam, A.H. Reshak, Mater. Sci. Semicond. Process. 26 (2014) 649–656.
[50] Wilayat Khan, A.H. Reshak, J. Mater. Sci. 49 (2014) 1179–1192.
[51] Wilayat Khan, A.H. Reshak, Comput. Mater. Sci. 89 (2014) 52–56.
[52] Wilayat Khan, A.H. Reshak, Sci. Adv. Mater. 6 (2014) 1716–1726.
[53] G.S. Nolas, D. Johnson, D.G. Mandrus. 2002, Thermoelectric materials and devices, in: Proceedings of the Materials Research Society. Warrendale, PA, vol. 691, 2002.
[54] T.M. Tritt (Ed.), Semiconductors and Semimetals: Recent Trends in Thermoelectric Materials Research, 69–71, Academic Press, San Diego, 2000.
[55] T.M. Tritt, M.G. Kanatzidis, H.B. Lyon, G.D. Mahan. (Eds.), New material for small-scale thermoelectric refrigeration and power generation applications. Proc, 545, Materials Research Society, Warrendale, PA, 1998, p. 1998. (Vol).
[56] T.M. Tritt, M.G. Kanatzidis, H.B. Lyon, G.D. Mahan. (Eds.), Thermoelectric materials—new directions and approaches: in: Proceedings of the Materials Research Society, vol. 478, Warrendale, PA, 1997.
[57] F.J. DiSalvo, Science 285 (1999) 703–706.
[58] D.M. Rowe, CRC Handbook of Thermoelectrics, CRC Press, 1995.
[59] X.C.C. Tong, Advanced Materials for Thermal Management of Electronic Packaging, Springer, 2011.